JOURNAL OF AIRCRAFT
Vol. 43, No. 4, July–August 2006

Detached-Eddy Simulation of Three Airfoils with Different Stall Onset Mechanisms

Dong Li*
Northwestern Polytechnical University, 710072 Xi'an, People's Republic of China
and
Igor Men'shov† and Yoshiaki Nakamura‡
Nagoya University, Nagoya 464-8603, Japan

The detached-eddy-simulation (DES) method is applied to calculate prestall and poststall aerodynamic characteristics of three airfoils that have different flow separation patterns at the stall regime. The DES method combines strong points of two turbulent models that are based on time-averaged and space-filtered Navier–Stokes equations, respectively. Specifically, we employ the Spalart–Allmaras DES approach, which has a Reynolds-averaged Navier–Stokes formulation near wall and reduces to a subgrid turbulence model, if we go away from the wall. The comparison between experimental data and numerical results is presented, which shows that the stall angle and prestall and poststall aerodynamic characteristics can be predicted by the present method accurately for two airfoils: NACA63_1-012 and NACA63_3-018. However, a discrepancy between numerical and experimental data is observed for the third airfoil: NACA64_A-006. The reason for this discrepancy and also possible improvements of the numerical model are discussed.

Nomenclature

C	=	airfoil chord length
C_D	=	drag coefficient
C_L	=	lift coefficient
C_M	=	momentum coefficient
d	=	wall distance
$\tilde{d}$	=	length scale
M_∞	=	freestream Mach number
α	=	angle of attack
Δ	=	local grid size
Δt	=	time step
υ	=	molecular viscosity coefficient
υ_t	=	turbulent viscosity coefficient
$\tilde{\upsilon}$	=	turbulence model variable

Introduction

IN the massive three-dimensional separation zones, which are typical for vehicles and airplane components, turbulence models based on the Reynolds-averaged Navier–Stokes (RANS) equations are not appropriate because dominant "detached" eddies in massively separated flows are highly geometry specific and have little attitude to the fairly universal turbulence model calibration.[1] On the other hand, recent estimates of the large-eddy-simulation (LES) approach for an airplane[2] show that because of the presence of thin near-wall turbulent boundary layers populated with small "attached" eddies, whose local size is much less than the boundary-layer thickness, the cost required exceeds presently available computational powers by orders of magnitude. As a result, there is no real prospect of using the LES for complex engineering computations in the near future.

Received 24 April 2005; revision received 17 August 2005; accepted for publication 23 August 2005.

*Postdoctoral Research Associate, Department of Aerospace Engineering.
†Associate Professor, Department of Aerospace Engineering. Member AIAA.
‡Professor, Department of Aerospace Engineering. Member AIAA.

To satisfy the need of computing massively separated turbulent flows in practical geometries and at practical Reynolds numbers, Spalart et al.[3] proposed the detached-eddy-simulation (DES) approach that aims to develop a practically realizable and accurate numerical model by combining the most favorable elements of the RANS and the LES models. The primary advantage of the DES method is its applicability to high-Reynolds-number flows (as RANS techniques) and capability to resolve geometry-dependent unsteady three-dimensional large-scale turbulent motions (as LES techniques).

The DES approach has been successively applied to a delta-wing vortex breakdown,[4] a supersonic axisymmetric base flow,[5] a circular cylinder, an airfoil pitch-up, and real configurations of several aircraft,[6] etc. The mentioned works focus on practical Reynolds numbers that are close to real flight conditions.

The DES results obtained in numerical experiments with the delta wing were compared with RANS results in Ref. 4. It was shown that although the RANS model well predicts the vortex breakdown phenomenon in general it does not improve the results concerning aerodynamic characteristics as more fine grids are implemented, whereas the DES model does show such improvements.

In the supersonic axisymmetric base-flow simulation with DES method,[6] both the boundary layer on the body surface and the wake-separated flow in the base region were well predicted. A smooth transition from the RANS region to the LES region is observed in this simulation as the flow separates from the body. The RANS approach again turns on once the flow is attached.

The DES and RANS calculations have been also compared for a practical problem of a fighter at high angles of attack.[7] Three grids of different densities are employed in these calculations. At all of the grids, the DES approach yields more accurate results for the lift force in comparison with those of the RANS calculations. Moreover, the grid refinement improves the lift force accuracy in the DES, but no such improvement is obtained in the RANS simulations.

As it was shown in Refs. 5 and 6, with available current computer resources, DES methods provide a good numerical tool to handle practical problems in aviation, which involve massively separated flows. For example, the calculation of axisymmetric base flow of a Reynolds number of 4.5×10^6 with 2.75 million grid points on 256 processors requires 30 wall clock hours.[5] For a real configuration of aircraft, the calculation with three million grid points and 432 SP3 processors requires 12.5 hours and gives rather reliable results. A fine grid of 10 million points requires four-days calculations on

256 processors and yields results within 5% difference with the flight-test data.[5] Thus, the DES method can be presently considered as a practical method for massively separated flows in aircraft engineering.

The present research is a response to the Computational-Fluid-Dynamics workshop on "Airfoil Stall Prediction" proposed by the National Aerospace Laboratories of Japan. During the workshop, results from several research teams have been announced.[8] For prestall flow regimes, almost all of the contributors have shown results that match experimental data fairly well. However, it was found that difficulties exist to predict the stall angle and poststall lift coefficients by using RANS simulations with different turbulence models, yet some researchers showed that adjusting the model parameters or the transition point location can somehow improve the result. Understanding that the RANS approach is limited in the application to massively separated flows in complicated geometry configurations, in the present research we try to implement the DES method with the aim to improve the prediction of stall and poststall aerodynamical characteristics.

Computational Method

Basic Equations

The Navier–Stokes equations can be written in the integral conservative form as follows:

$$\frac{\partial}{\partial t}\iiint_{\Omega} \boldsymbol{w}\,\mathrm{d}\Omega + \iint_{\partial\Omega} \boldsymbol{f}_j \cdot n_j\,\mathrm{d}s = \iint_{\partial\Omega} \boldsymbol{g}_j \cdot n_j\,\mathrm{d}s \qquad (1)$$

where $\boldsymbol{w}$ is the state vector of conservative variables, $\boldsymbol{f}_j$ and $\boldsymbol{g}_j$, $j = 1, 2, 3$ are inviscid and viscous fluxes, respectively. Discretized with the finite volume method, these equations take the following form:

$$\frac{\mathrm{d}}{\mathrm{d}t}\boldsymbol{w}_i + \sum_j \boldsymbol{R}(\boldsymbol{w}_i, \boldsymbol{w}_j) = 0 \qquad (2)$$

where $\boldsymbol{R}$ denotes the approximation of inviscid and viscous fluxes at interfaces surrounding a current cell i.

The pseudo-time-stepping method[9] is then applied to Eq. (2) where the fully implicit second-order time-integration scheme is used in physical time. This leads to the following system of ordinary differential equations:

$$\frac{\mathrm{d}}{\mathrm{d}\tau}\boldsymbol{w}_i^{n+1} + \frac{3\boldsymbol{w}_i^{n+1} - 4\boldsymbol{w}_i^{n} + \boldsymbol{w}_i^{n-1}}{2\Delta t} + \sum_j \boldsymbol{R}\left(\boldsymbol{w}_i^{n+1}, \boldsymbol{w}_j^{n+1}\right) = 0 \qquad (3)$$

where τ denotes pseudotime.

To integrate Eq. (3) in pseudotime, the five-stage Runge–Kutta method is employed. The local time stepping and the artificial residual smoothing are used to accelerate the convergence to the steady-state solution in pseudotime.

Turbulence Model

We use the Spalart–Allmaras one-equation turbulence model.[10] In this model, the following partial differential equation is solved for the variable $\tilde{\upsilon}$:

$$\frac{\mathrm{D}\tilde{\upsilon}}{\mathrm{D}t} = c_{b1}[1 - f_{t2}]\tilde{S}\tilde{\upsilon} - \left[c_{w1} f_w - \frac{c_{b1}}{\kappa^2} f_{t2}\right]\left[\frac{\tilde{\upsilon}}{d}\right]^2 + \frac{1}{\sigma}\left\{\nabla\cdot[(\upsilon + \tilde{\upsilon})\nabla\tilde{\upsilon}] + c_{b2}(\nabla\tilde{\upsilon})^2\right\} + f_{t1}\Delta U^2 \qquad (4)$$

The right-hand side of Eq. (4) contains production, destruction, and diffusion terms. The parameter that defines the production term is given by

$$\tilde{S} \equiv S + (\tilde{\upsilon}/\kappa^2 d^2) f_{v2}, \qquad f_{v2} = 1 - \chi/(1 + \chi f_{v1})$$

with

$$f_{v1} = \chi^3/\left(\chi^3 + c_{v1}^3\right), \qquad \chi \equiv \tilde{\upsilon}/\upsilon$$

Here S is the magnitude of vorticity, and d is the minimal distance to the wall.

The functions f_w and f_{t2} are given by the following expressions:

$$f_w = g\left[\frac{1 + c_{w3}^6}{g^6 + c_{w3}^6}\right]^{\frac{1}{6}}, \qquad f_{t2} = c_{t3}\exp\left(-c_{t4}\chi^2\right)$$

with

$$g = r + c_{w2}(r^6 - r), \qquad r \equiv \tilde{\upsilon}/\tilde{S}\kappa^2 d^2$$

The boundary condition at the wall is set as $\tilde{\upsilon} = 0$. The constants in the foregoing equations are

$$c_{b1} = 0.1355, \qquad \sigma = \tfrac{2}{3}, \qquad c_{b2} = 0.622, \qquad \kappa = 0.41$$

$$c_{w1} = c_{b1}/\kappa^2 + (1 + c_{b2})/\sigma, \qquad c_{w2} = 0.3, \qquad c_{w3} = 2$$

$$c_{v1} = 7.1, \qquad c_{t1} = 1, \qquad c_{t2} = 2, \qquad c_{t3} = 1.1, \qquad c_{t4} = 2$$

Once $\tilde{\upsilon}$ is calculated, the turbulent viscosity is determined by $\upsilon_t = \tilde{\upsilon} f_{v1}$

Detached-Eddy Simulation

The DES is a new approach that has been recently proposed to treat massively separated turbulent flows. In its original formulation,[3] the DES model reads as a modification of the Spalart–Allmaras RANS model, which turns the latter into a subgrid-scale turbulence model as we move away from the solid walls. In this manner the DES method combines the RANS technology in attached boundary layers and the LES approach aimed to resolve detached eddies in massively separated flows.

The DES formulation is obtained by replacing the distance to the nearest wall in the Spalart–Allmaras RANS model d, by $\tilde{d}$, which is defined by

$$\tilde{d} \equiv \min(d, C_{\mathrm{DES}}\Delta) \qquad (5)$$

where Δ represents the local grid size, which is taken as the largest distance among the distances between the current cell center and the centers of its neighbors. The threshold parameter C_{DES} is taken in the present study as $C_{\mathrm{DES}} = 0.65$. With the Eq. (5), the computational domain is typically divided into two regions: the RANS region where the real distance d is used and the LES region where the wall distance in the RANS model is substituted with the local grid scale. One example of such a division is shown in Fig. 1 for a C-H type grid around an airfoil, which is displayed in Fig. 2. One can see that the RANS region is localized in a thin layer near the airfoil surface. Outside this layer, the model switches to the LES counterpart.

Numerical Solution Procedure

We extend the implicit time-integration method to solve the turbulence transport model equations (4) and (5) within the Navier–Stokes solver.

The last term on the right-hand side of Eq. (4) defines the transition from laminar to turbulent regimes. This term is not taken into account in the present study. With the mass-balance equation, Eq. (4) can be recast in the following conservative form:

$$\frac{\partial}{\partial t}\rho\tilde{\upsilon} + \partial_k(\rho\tilde{\upsilon}u_k) = \frac{1}{\sigma}\partial_k\{[\rho\upsilon + \rho(1 + C_{b2})\tilde{\upsilon}]\partial_k\tilde{\upsilon}\} - \tilde{\upsilon}\frac{C_{b2}}{\sigma}\partial_k[\rho\partial_k\tilde{\upsilon}] + A_1\tilde{\upsilon} + A_2\tilde{\upsilon}^2 \qquad (6)$$

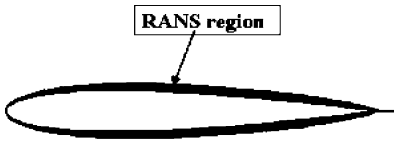

Fig. 1 Splitting the computational domain into RANS and LES regions.

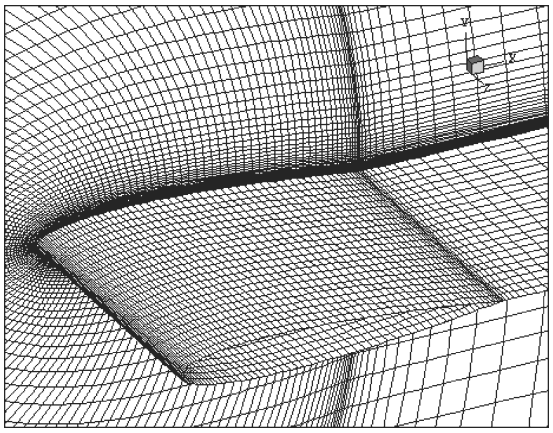

Fig. 2 Partial view of grid for NACA63$_3$-018.

Discretization of this equation by the finite volume method yields

$$\rho\Omega_i\frac{\partial\tilde{\upsilon}_i}{\partial t}=-\sum_\sigma S_\sigma\rho_\sigma\left[u^+_{n,i}\tilde{\upsilon}_i+u^-_{n,\sigma(i)}\tilde{\upsilon}_{\sigma(i)}\right]$$

$$+\frac{1}{\sigma}\sum_\sigma S_\sigma[\rho_\sigma\upsilon_\sigma+\rho_\sigma(1+C_{b2})\tilde{\upsilon}_\sigma](\partial_n\tilde{\upsilon}_i)_\sigma$$

$$-\tilde{\upsilon}_i\frac{C_{b2}}{\sigma}\sum_\sigma S_\sigma\rho_\sigma(\partial_n\tilde{\upsilon})_\sigma+\left(A_1\tilde{\upsilon}_i+A_2\tilde{\upsilon}_i^2\right)\Omega_i \tag{7}$$

where Ω_i is the cell volume, S_σ is the interface area, σ denotes the interface between the ith cell and its neighbor cell, which is denoted by $\sigma(i)$, the subscripts denotes the vector component normal to the interface, and by the summation is performed over all interfaces surrounded by the ith cell.

The $-$ and $+$ splitted parts of the velocity are defined by

$$u^+=0.5(u+|u|),\qquad u^-=0.5(u-|u|)$$

Applying the implicit time-integration scheme to Eq. (7), one can obtain the following discrete equation for $\tilde{\upsilon}^{n+1}$:

$$\frac{\rho\Omega_i}{\Delta t}\Delta\tilde{\upsilon}_i=-\sum_\sigma S_\sigma\rho_\sigma\left[u^+_{n,i}\tilde{\upsilon}_i^{n+1}+u^-_{n,\sigma(i)}\tilde{\upsilon}^{n+1}_{\sigma(i)}\right]$$

$$+\sum S_\sigma\Gamma_{\mathrm{dis},\sigma}(\partial_n\tilde{\upsilon})^{n+1}_\sigma$$

$$+\left[A_1^+\tilde{\upsilon}_i^n+A_2^+\left(\tilde{\upsilon}_i^n\right)^2+A_1^-\tilde{\upsilon}_i^{n+1}+A_2^-\left(\tilde{\upsilon}_i^{n+1}\right)^2\right]\Omega_i \tag{8}$$

where

$$\Gamma_{\mathrm{dis},\sigma}=(1/\sigma)[\rho_\sigma\upsilon_\sigma+\rho_\sigma(1+C_{b2})\tilde{\upsilon}_\sigma-\tilde{\upsilon}_i\rho_\sigma C_{b2}]$$

$$\Delta\tilde{\upsilon}_i=\tilde{\upsilon}_i^{n+1}-\tilde{\upsilon}_i^n$$

The splitted coefficients $A_1^\pm$ and $A_2^\pm$ are determined by

$$A^\pm=0.5(A\pm|A|)$$

Equation (8) is solved with the Newton iterative method attended by the lower-upper symmetric Gauss-Seidel (LU-SGS) method as a linear system solver.[11] Letting s be the iteration index, the linear system is first written as

$$D_i^s\delta^s\tilde{\upsilon}_i=R_i^s-\sum_\sigma G_\sigma^s\delta^s\tilde{\upsilon}_{\sigma(i)} \tag{9}$$

where $\delta^s\tilde{\upsilon}_i=\tilde{\upsilon}_i^{n+1,s+1}-\tilde{\upsilon}_i^{n+1,s}$ is the iterative increment and R is the iterative residual defined by

$$R_i^s=-\frac{\rho\Omega_i}{\Delta t}\left(\tilde{\upsilon}_i^{n+1,s}-\tilde{\upsilon}_i^n\right)+\text{r.h.s of Eq. (8)}$$

Here the second term is the right-hand side of Eq. (8) calculated at $\tilde{\upsilon}^{n+1}=\tilde{\upsilon}^{n+1,s}$. The coefficients D and G in Eq. (9) have the following form:

$$D_i^s=\frac{\rho\Omega_i}{\Delta t}-\left(A_1^-+2A_2^-\right)\Omega_i+\sum_\sigma\left(\rho_\sigma u^+_{n,i}+\frac{\Gamma_{\mathrm{dis},\sigma}}{h_\sigma}\right)s_\sigma$$

$$G_\sigma^s=\left[\rho_\sigma u^-_{n,\sigma(i)}-\frac{\Gamma_{\mathrm{dis},\sigma}}{h_\sigma}\right]s_\sigma$$

where h_σ is the distance between centers of the ith cell and the $\sigma(i)$th cell.

Then, the linear system of Eq. (9) is solved by the LU-SGS method in two subsequent sweeps; forward (for $i=1,\ldots,N$) and backward (for $i=N,\ldots,1$), as follows:

$$\left(\delta^s\tilde{\upsilon}_i\right)^*=\left\{R_i^s-\sum_{\sigma:\sigma(i)<i}G_\sigma^s\left[\delta^s\tilde{\upsilon}_{\sigma(i)}\right]^*\right\}\Big/D_i^s$$

$$\delta^s\tilde{\upsilon}_i=\left(\delta^s\upsilon_i\right)^*-\sum_{\sigma:\sigma(i)>i}G_\sigma^s\delta^s\tilde{\upsilon}_{\sigma(i)}/D_i^s$$

Numerical Results and Comparison to Experiment

The following three airfoils[12] with different stall onset mechanisms are selected for this study: NACA63$_3$-018 characterized by the trailing-edge stall; NACA63$_1$-012 characterized by the leading-edge stall; and NACA64A-006 with typical thin airfoil stalling.

The calculations are performed for a Reynolds number of 5.8E10^6 and a Mach number of 0.3. The grid is shown in Fig. 2. It has 201 points in the streamwise direction, 81 points normal to the wing surface, and 25 in the spanwise direction, respectively.

All calculations presented next are carried out for a subsonic flow regime that is characterized by a freestream Mach number $M_\infty=0.3$. The length scale is taken to be equal to the chord length of the airfoil. The reference pressure and density are the pressure and density at infinity, respectively. Then, the timescale defined as $T_{\mathrm{ch}}=c/V_\infty$, where c is the chord length, equals 2.82 in nondimensional variables.

A typical time history of lift coefficient is shown in Fig. 3. Here the lift coefficient is given for the airfoil NACA64A-006 at an angle of attack of $\alpha=8$ deg. Time-averaged values of the lift coefficient for different time periods (shown in the figure by arrows) are also displayed by markers. One can see that the time required for the lift coefficient to converge is $T\approx 30T_{\mathrm{ch}}$ from the initial moment. The initial data are set to be equal to freestream parameters for all calculations presented.

NACA63$_1$-012 Airfoil

The onset of the stall region for this type of airfoil is characterized by the flow separation that occurs near the leading edge. As the angle of attack increases, the flow suddenly separates in the vicinity of the leading edge. The separation region extends over all of the upper surface of the airfoil, which leads to a lift loss at angles of attack greater than the stall angle.

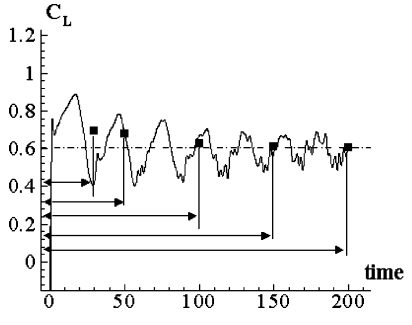

Fig. 3 Time history of lift coefficient; markers denote averaged values.

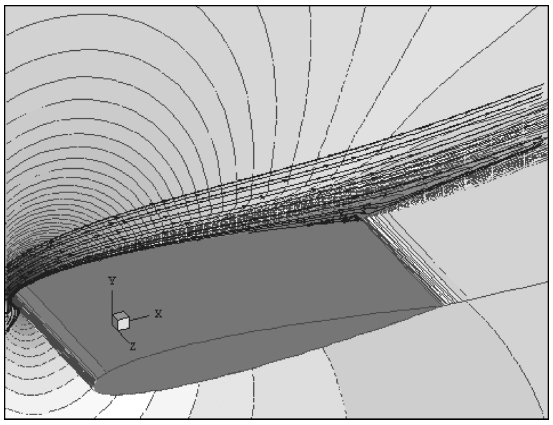

a) $\alpha = 14$ deg

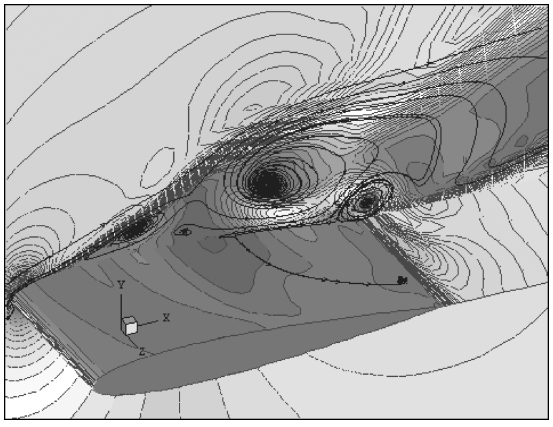

b) $\alpha = 15$ deg

Fig. 4 Pressure contours and streamlines for NACA63$_1$-012 at two different angles of attack.

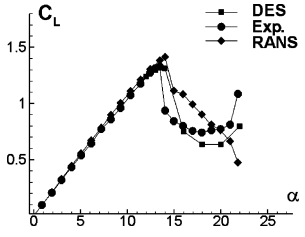

Fig. 5 Lift coefficient vs angle of attack for NACA63$_1$-012.

Three-dimensional calculations are performed for a finite-plane wing with the cross section of the NACA63$_1$-012 airfoil. The wing span is equal to the length of the chord. The periodical boundary conditions are imposed in the spanwise direction. The angle of attack α is gradually changed in calculations from zero to stall and poststall values.

Figures 4a and 4b illustrate typical flowfields at a prestall and a poststall angle of attack, respectively. At $\alpha = 14$ deg, the flow is attached to the airfoil (see Fig. 4a), while it separates from the leading edge with making a large vortical structure on the upper part of the airfoil as α reaches a value of 15 deg (see Fig. 4b). Also, the attached flow ($\alpha = 14$ deg) is nearly two dimensional, while the flow separation ($\alpha = 15$ deg) destroys completely the two dimensionality and the flow shows essential three-dimensional features (see the pressure contours on the upper surface of the wing in Fig. 4b).

In our previous study[13] we showed that by using only RANS models are we able to predict prestall lift characteristics well and capture the stall angle adequately. However, this approach fails to predict the poststall aerodynamical characteristics.

In Fig. 5 we show the comparison between experimental lift coefficient[12] and averaged numerical lift coefficient at different angles of attack. The numerical results are given for calculations with the DES approach and the RANS model, respectively. One can see that both the numerical data match the experimental data quite well for $\alpha \leq \alpha_{\text{stall}} = 14$ deg. At higher angles of attack, the RANS model data greatly deviate from the experimental data, whereas the DES results can match them quite well.

NACA63$_3$-018 Airfoil

The lift loss at poststall regimes is caused in this case by the flow separation near the trailing edge, which extends rather slowly toward the upstream as the angle of attack increases. This process is illustrated in Figs. 6a and 6b, where pressure contours and streamlines are shown for two angles of attack just after the stall angle.

The numerical results of lift coefficient show only a minor difference between the RANS and DES models and the experimental data as well, as one can see in Fig. 7. This means that, for weakly separated flows, use of the RANS turbulence model can provide reliable results.

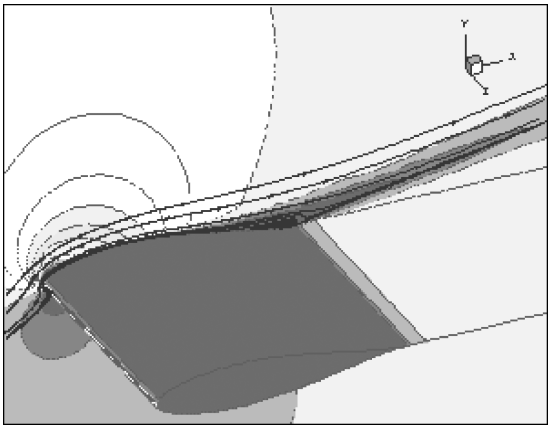

a) $\alpha = 15$ deg

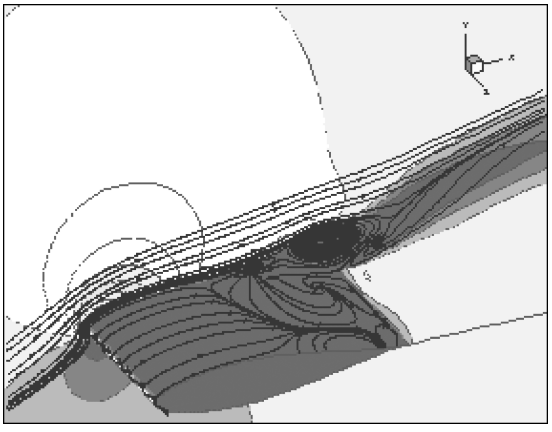

b) $\alpha = 16$ deg

Fig. 6 Pressure contours and streamlines for NACA63$_3$-018 at two poststall angles of attack.

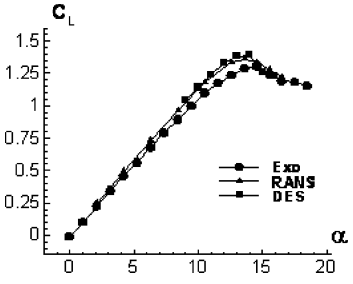

Fig. 7 Lift coefficient vs angle of attack the NACA63$_3$-018.

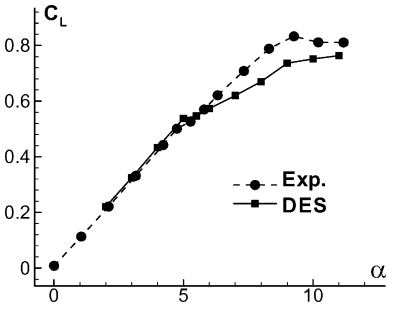

Fig. 8 Lift coefficient vs angle of attack for NACA64A-006.

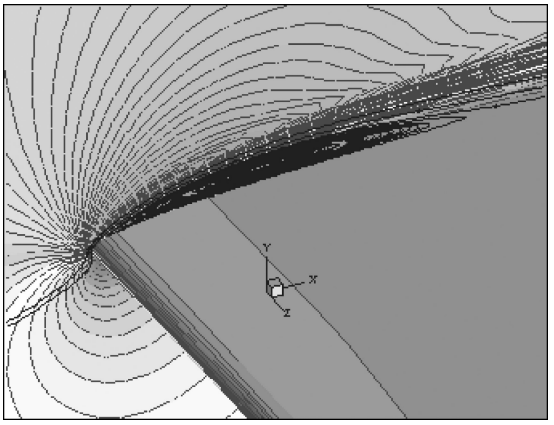

a) $\alpha = 5.27$ deg

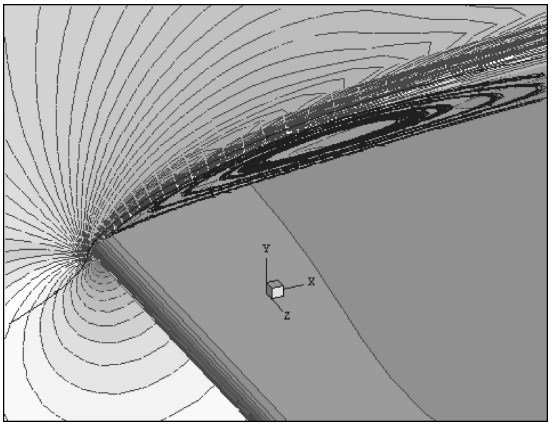

b) $\alpha = 6$ deg

Fig. 9 Pressure contours and streamlines for NACA64A-006.

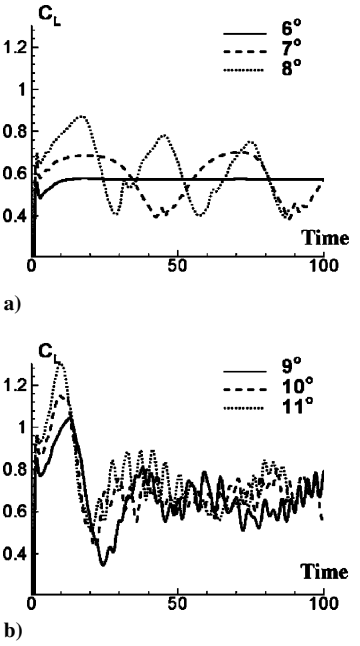

a)

b)

Fig. 10 Time history of lift coefficient for angles attack from $\alpha = 7$ to 11 deg (NACA64A-006).

NACA64A-006 Airfoil

For this type of airfoil, as the angle of attack increases, first a separated bubble appears on the upper surface near the leading edge. This occurs at $\alpha \approx 5.27$ deg and leads to a nonlinear behavior in the lift coefficient vs angle of attack, as we can see in Fig. 8. The appearance of the bubble near the leading edge is illustrated in Figs. 9a and 9b, where computed contours of pressure and streamlines are shown for $\alpha = 5.27$ and 6 deg, respectively.

The time history of lift coefficient is shown in Figs. 10a and 10b for angles of attack $\alpha = 6$, 7, 8 deg, and 9, 10, 11 deg, respectively. One can see that the behavior of the lift coefficient with time is drastically changed as the angle of attack increases. At $\alpha = 6$ deg, the flowfield is stationary and nearly two dimensional, whereas at $\alpha = 7$ deg it becomes unsteady with a periodical character that can be seen in Fig. 10a. Further increase in angle of attack destroys this periodicity. Although at $\alpha = 8$ deg the flow is still nearly periodical, at $\alpha = 9$, 10, and 11 deg it loses any periodicity and shows a typical turbulent behavior.

Figure 11 displays the flowfield for four different instants at $\alpha = 8$ deg. The bubble near the leading edge is not stable in this case; it breaks into smaller bubbles, and then the flow almost reattaches the upper surface. After this the flow separation begins again with the formation of a new leading-edge bubble. This process is periodically repeated.

Figure 8 shows averaged lift coefficient vs angle of attack. One can see that discrepancy in the lift force between the numerical results and experimental data emerges as the angle of attack exceeds the angle of the onset of flow separation on the upper surface ($\alpha = 5.27$ deg). This discrepancy becomes more severe with increasing of the angle of attack, which indicates that the DES model is not accurate enough to predict adequately the lift characteristics at prestall and poststall regimes.

Effects of Parameters and Improvements in Simulating Thin Airfoil Stalling

As was already mentioned, the unsteadiness in the flow appears far before the stall in the case of thin airfoil because the bubble destabilization phenomenon occurs near the leading edge. After that, some discrepancy is observed in the lift characteristics between experimental and numerical data. In this section, we discuss several factors that can affect the accuracy of numerical simulations and propose some modifications which can improve numerical results for unsteady regimes of thin airfoils.

Effect of Time Step

Two calculations are carried out to examine and analyze the effect of time step: with $\Delta t = 0.1$ and 0.05, which correspond to the time required for the upstream flow to pass over a length of 3.5 and 1.8% of the chord length, respectively. The calculations are performed for $\alpha = 8$ and 11 deg that are in before- and after-stall regimes, respectively.

In Fig. 12 we show the time histories of lift coefficient for these simulations. One can see that for the prestall regime of $\alpha = 8$ deg, the use of different time steps leads to almost same results (see Fig. 12a). However, the situation has changed at the poststall regime of $\alpha = 11$ deg; no replica of the time history is observed when the time step is half reduced, yet the results are close enough. This seems to be the effect of the small turbulent structures that cannot be properly resolved by the DES with the grid used in the present calculations, but can affect the resolved flowfield.

The time-averaged lift, drag, and momentum coefficients are listed in Table 1. One can see that the effect of unresolved structures is not so large; poststall characteristics ($\alpha = 11$ deg) show that the

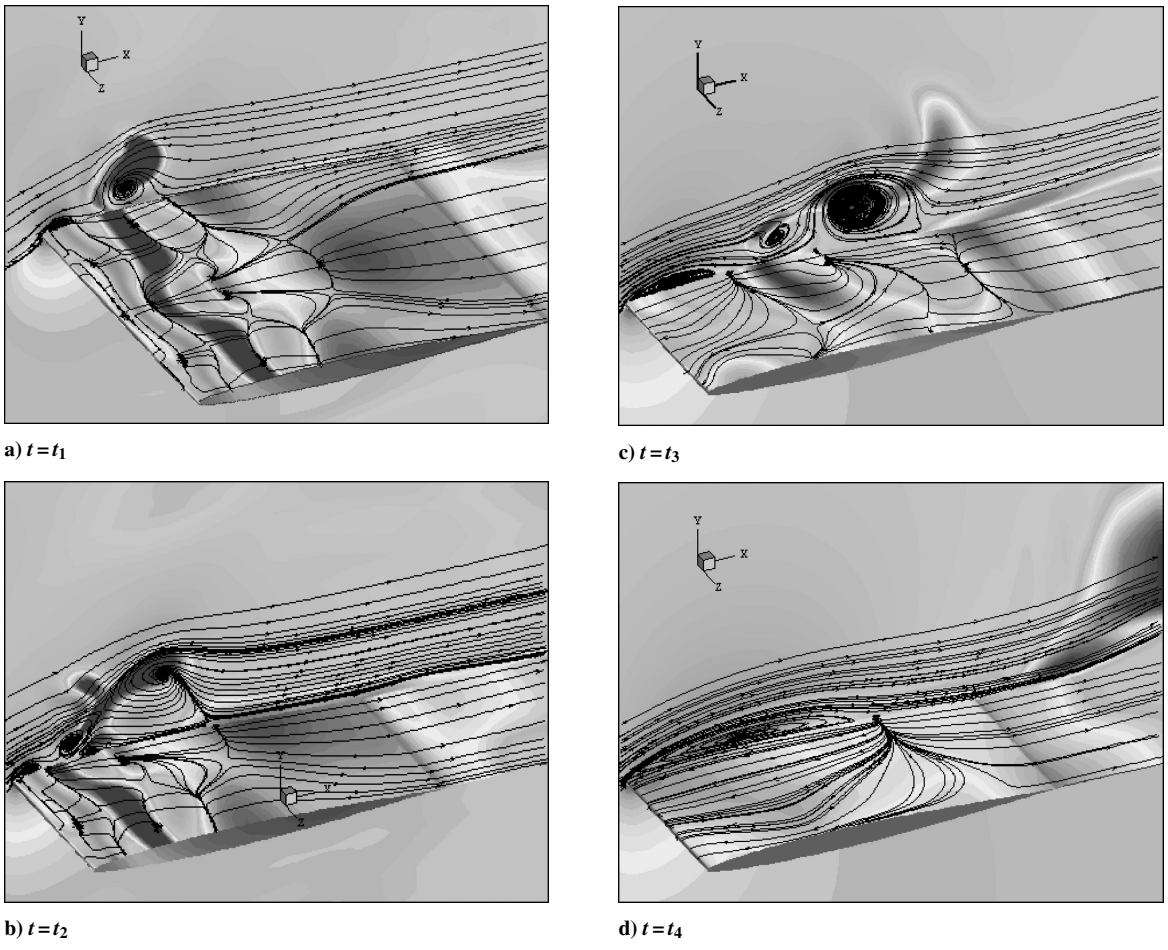

a) $t = t_1$ c) $t = t_3$

b) $t = t_2$ d) $t = t_4$

Fig. 11 Pressure contours and streamlines at different instants for $\alpha = 8$ deg (NACA64A-006).

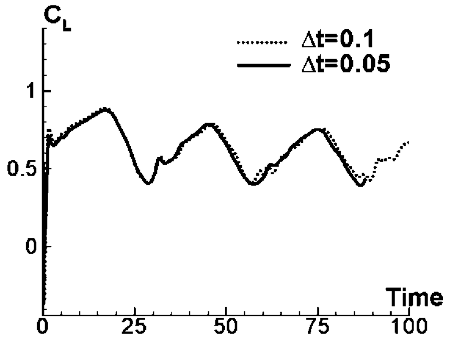

a) $\alpha = 8$ deg

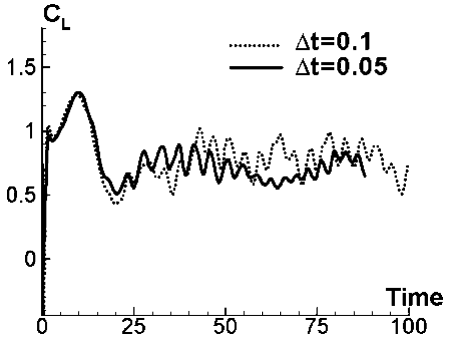

b) $\alpha = 11$ deg

Fig. 12 Effect of time step on the time history of lift coefficient.

Table 1 Dependence of averaged coefficients on time step

Time step	C_L	C_D	C_M
	$\alpha = 8$ deg		
EXP	0.76	0.098	−0.03
$\Delta t = 0.1$	0.604	0.085	−0.047
$\Delta t = 0.05$	0.606	0.086	−0.050
	$\alpha = 11$ deg		
EXP	0.81	0.18	−0.11
$\Delta t = 0.05$	0.783	0.169	−0.121
$\Delta t = 0.1$	0.763	0.157	−0.096

difference is a few percent between the calculations with different time steps. Therefore, for the rest of this paper we adopt $\Delta t = 0.1$.

Effect of the Number of Inner Iterations

In the present work, the explicit local time-stepping method is used in inner iterations in pseudotime to update the solution to a new physical time level. To examine the effect of the number of inner iterations on results, three different calculations are carried out where the inner iterations are executed 2, 20, and 40 times, respectively. The calculations are performed for an angle of attack of 8 deg. Initial conditions are set in the form of uniform flow. The corresponding time histories of lift coefficient are shown in Fig. 13. As we can see, the calculations with 20 and 40 inner iterations show only a minor difference in the lift-time behavior. However, using only a few iterations seems to be not legitimate and leads to a wrong solution. Therefore, a number of 20 inner iterations is employed in the rest of the paper.

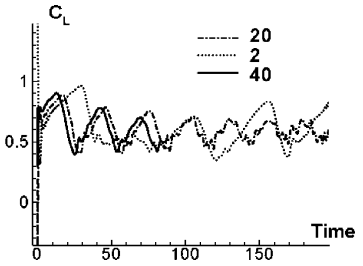

Fig. 13 Effect of the number of inner iterations.

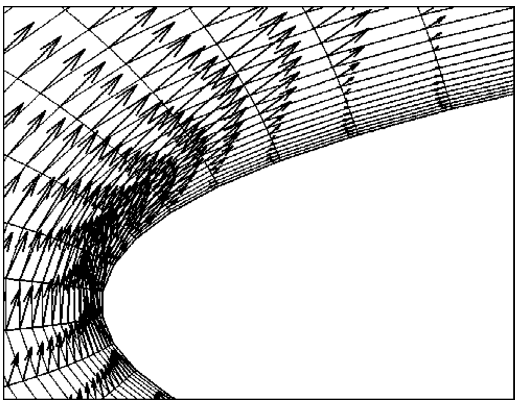

Fig. 14 Grid and velocity field near the leading edge.

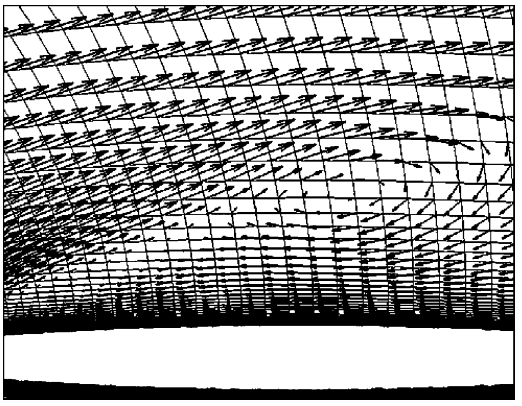

Fig. 15 Grid and velocity field near the separation region.

Effect of Grid Density

Because the DES method includes the LES model as a part of the calculation, the grid density can play an important role. Figure 14 shows a close-up of the onset of the flow separation for the airfoil NACA64A-006 ($\alpha = 6$ deg). One can see that this region is discretized with a sufficient number of cells in the plane normal to the spanwise.

Figure 15 shows a close-up of the separation region in the flow around airfoil NACA64A-006 ($\alpha = 8$ deg). As can be seen, the separation flow is discretized with sufficient grid resolution in the plane normal to the spanwise.

The grid size in the spanwise direction affects the separation between the RANS region and the LES region. [We recall that the length scale is defined as the smallest value between the wall distance and the local grid size, Eq. (5)].

To analyze the effect of grid density on numerical results, we perform two calculations with different grids. One grid has the cell size in the spanwise direction $\Delta z = 0.04$, and the other is half less, $\Delta z = 0.02$. The time history of lift coefficient in these calculations is shown in Figs. 16a and 16b for angles of attack $\alpha = 7$ and 8 deg, respectively.

Two different situations can be seen from these calculations. At smaller angle of attack $\alpha = 7$ deg, the numerical result is nearly reproduced when the grid in the spanwise direction is halved. On the other hand, the result becomes grid dependent as the angle of attack is raised to $\alpha = 8$ deg. This fact can point to the presence of turbulent structures in the spanwise direction, which are too small to be resolved with a coarse grid of $\Delta z = 0.04$, but large enough to affect the lift coefficient.

Table 2 Dependence of averaged coefficients on spanwise grid spacing

$\alpha = 8$ deg	C_L	C_D	C_M
EXP	0.76	0.098	−0.03
$\Delta z = 0.04$	0.604	0.085	−0.047
$\Delta z = 0.02$	0.651	0.095	−0.070

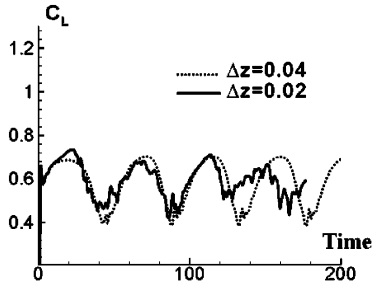

a) $\alpha = 7$ deg

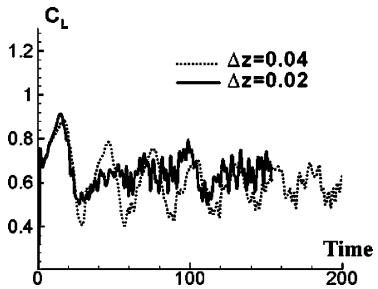

b) $\alpha = 11$ deg

Fig. 16 Effect of grid spacing in the spanwise direction.

Time-averaged lift, drag, and momentum coefficients are listed in Table 2. For comparison, the experimental data[12] are also given. We can see that these numerical results are modified as the grid becomes twice as dense, with the results of the finer grid ($\Delta z = 0.02$) being closer to experimental values.

Effect of Turbulence Modeling in the RANS Region

The presence of an unsteady bubble in the vicinity of the leading edge is an essential structure of the prestall flow around thin airfoils. This structure should be properly resolved in numerical simulations in so far as it strongly influences the flow separation process on the upper surface of the wing and hence aerodynamical lift and drag.

The flow in the bubble region is affected by the shear layer in the close proximity to the wall. Therefore, proper modeling of turbulence in the RANS region is of crucial importance for this case.

This section concerns the effect of turbulence modeling the wall-adjacent flow on numerical results. We examine a different turbulence model of the RANS region, to be exact—the Baldwin–Lomax model,[14] which is known to give very good results specifically for attached wall-confined flows. Thus, the turbulence model to be used in this section is a modification of the DES approach that is based on Eqs. (4) and (5), where the Spalart–Allmaras equation with the modified wall distance parameter $\tilde{d}$ is used for the LES region, while the Baldwin–Lomax model is used for the RANS region. The separation between the two regions is fulfilled as before, that is, by means of Eq. (5).

The calculations are performed with the same grid of $\Delta z = 0.04$. The time histories of lift coefficient for the angle of attack $\alpha = 8$ deg are presented in Fig. 17. The curves correspond to the DES model based on entirely the Spalart–Allmaras model (SA) and on the Spalart–Allmaras model implemented with the Baldwin–Lomax model (SA+BL) for the RANS region, respectively.

As can be seen from Fig. 17, lift coefficients given by the SA model and SA+BL model deviate from each other after some initial

Table 3 Effect of RANS turbulence modeling on averaged aerodynamic coefficients

$\alpha = 8$ deg	C_L	C_D	C_M
EXP	0.76	0.098	−0.03
DES(SA)	0.604	0.085	−0.047
DES(BL+SA)	0.705	0.100	−0.066

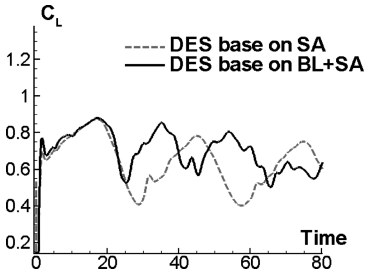

Fig. 17 Effect of turbulence modeling in RANS region.

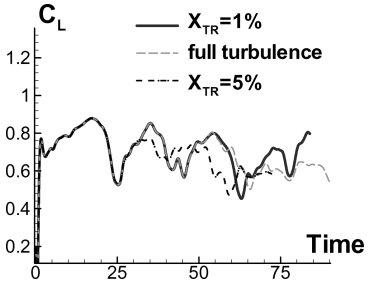

Fig. 18 Effect of transition modeling.

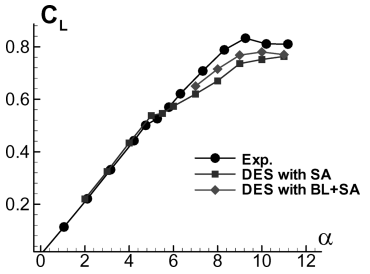

Fig. 19 Lift coefficient vs angle of attack for NACA64A-006.

time. The minimal lift coefficient in the BL+SA calculation appears to be larger than that in the SA calculation. In Table 3 we list the time-averaged lift, drag, and momentum coefficients in the SA and SA+BL calculations. One can see that using the BL model instead of the SA model in the RANS region leads to higher averaged values that better agree with experimental data. Thus, specific modeling of turbulence in RANS regions seems to be a promising DES approach and needs more study.

Effect of Transition Modeling

The foregoing results correspond to the fully turbulent case without implementing any transition models. To take into account the effect of turbulent transition, two calculations are performed with the BL+SA model with the transition point to be set at a distance from the leading edge of 1% and 5% of the chord length, respectively. The lift coefficients obtained in these calculations are displayed in Fig. 18.

One can see that the 1% transition model improves numerical results; the averaged lift coefficient increases in comparison with that of the fully turbulent case. On the other hand, too large a delay in transition might deteriorate the situation; the calculation with the 5% transition model shows a lower value of the averaged lift coefficient so that the agreement between numerical and experimental data worsens.

In Fig. 19 we show the improvement that can be achieved in the DES lift prediction by means of foregoing modifications. The lift curves (lift coefficient vs angle of attack) presented in this figure are experimental data and two numerical data. The numerical curves were obtained with the baseline fully turbulent SA DES model and with the 1% transition SA+BL DES model, respectively. One can see that taking into account the transition model and improving the turbulence model of the RANS region can reduce discrepancy of experiment to calculation by a third.

Conclusions

In this study, three airfoils with different stall onset mechanisms have been numerically simulated by using the DES approach and RANS approach.

1) For the NACA63_3-018 airfoil, the lift loss at the stall regime is caused by the flow separation near the trailing edge. The separation region slowly extends toward upstream as the angle of attack increases. A minor difference is observed between the RANS and DES methods. Thus, for slightly separated flows the use of RANS models can provide reliable results.

2) In the case of NACA63_1-012 airfoil, as the angle of attack increases the flow suddenly separates in the vicinity of the leading edge. The separation region extends over all of the upper surface of the airfoil. This leads to a sudden loss of lift at poststall regimes. Before the stall, both the RANS and DES methods yield quite reliable results. However, after the stall the DES results agree much better with experimental data than the RANS results. These results point to the ability of the DES method to handle massively separated flows.

3) For the NACA64A-006 airfoil, a difference between DES numerical results and experimental data appears yet before the stall, which becomes severe at stall and poststall regimes. This occurs as a result of a bubble that is created near the leading edge. The bubble is destabilized as the angle of attack is increased, and the flow becomes unsteady and highly turbulent. Refining the grid in the spanwise direction affects the numerical results in this case and shows the trend from quasi-periodical to a turbulent behavior. It has been shown that the use of the Baldwin–Lomax model in the RANS region and inclusion of the transition model improves the DES results. With taking these factors into account, the DES approach could reliably predict stall aerodynamic characteristics.

References

[1]Strelets, M., "Detached Eddy Simulation of Massively Separated Flows," AIAA Paper 2001-0879, Jan. 2001.

[2]Spalart, P. R., "Trends in Turbulence Treatments," AIAA Paper 2000-2306, June 2000.

[3]Spalart, P. R., Jou, W.-H., Strelets, M., and Allmaras, S. R., "Comments on the Feasibility of LES for Wings, and on a Hybrid RANS/LES Approach," *Advances in DES/LES*, edited by C. Liu and Z. Liu, Greyden Press, Columbus, OH, Aug. 1997.

[4]Morton, S., Forsythe, J. R., Mitchell, A., and Hajek, D., "DES and RANS Simulations of Delta Wing Vortical Flows," AIAA Paper 2002-0587, Jan. 2002.

[5]Forsythe, J. R., Hoffmann, K. A., and Squires, K. D., "Detached-Eddy Simulation with Compressibility Corrections Applied to a Supersonic Axisymmetric Base Flow," AIAA Paper 02-0586, Jan. 2002.

[6]Squires, K. D., Forsythe, J. R., Morton, S. A., Strang, W. Z., Wurzler, K. E., Tomaro, R. F., Grismer, M. J., and Spalart, P. R., "Progress on Detached-Eddy Simulation of Massively Separated Flows," AIAA Paper 2002-1021, March 2002.

[7]Forsythe, J. R., Squires, K. D., Wurtzler, K. E., and Spalart, P. R., "Detached-Eddy Simulation of Fighter Aircraft at High Alpha," AIAA Paper 2002-0591, Jan. 2002.

[8]*Proceedings of Aerospace Numerical Simulation Symposium 2000*, Special Publication of National Aerospace Lab., NAL SP-46, Tokyo, 2000.

[9]Arnone, A., Liou, M. S., and Povinelli, L. A., "Integration of Navier–Stokes Equations Using Dual Time Stepping and a Multigrid Method," *AIAA Journal*, Vol. 33, No. 6, 1995, pp. 985–990.

[10]Spalart, P. R., and Allmaras, S. R., "A One-Equation Turbulence Model for Aerodynamic Flows," AIAA Paper 92-0439, Jan. 1992.

[11]Men'shov, I., and Nakamura, Y., "On Implicit Godunov Method with Exactly Linearized Numerical Flux," *Computer and Fluids*, Vol. 29, No. 6, 2000, pp. 695–616.

[12]George, B., and Donald, E., "Examples of Three Representative Types of Airfoil Section Stall at Low Speed," NACA Technical Report, TN-2502, Sept. 1951.

[13]Li, Dong, Men'shov, I., and Nakamura, Y., "2D RANS Simulation for Three Different Stall Types," *Proceedings of the 35th Fluid Dynamics Conference of Japan*, Japan Society of Fluid Mechanics, Kyoko Univ., Kyoko, Japan, 2003, pp. 56–59.

[14]Baldwin, B. S., and Lomax, H., "Thin Layer Approximation and Algebraic Model for Separated Turbulent Flows," AIAA Paper 78-0257, Jan. 1978.